Accepted Manuscript

A Model to Describe the Mechanical Behavior and the Ductile Failure of Hydrided Zircaloy–4 Fuel Claddings between 25 C and 480 °C

M. Le Saux, J. Besson, S. Carassou

PII: S0022-3115(15)30112-4

DOI: 10.1016/j.jnucmat.2015.07.026

Reference: NUMA 49226

To appear in: *Journal of Nuclear Materials*

Received Date: 23 March 2015

Revised Date: 8 July 2015

Accepted Date: 16 July 2015

Please cite this article as: M. Le Saux, J. Besson, S. Carassou, A Model to Describe the Mechanical Behavior and the Ductile Failure of Hydrided Zircaloy–4 Fuel Claddings between 25 C and 480 °C, *Journal of Nuclear Materials* (2015), doi: 10.1016/j.jnucmat.2015.07.026.

A Model to Describe the Mechanical Behavior and the Ductile Failure of Hydrided Zircaloy–4 Fuel Claddings between 25 °C and 480 °C

M. Le Saux[a,*], J. Besson[b], S. Carassou[a]

[a] *CEA, DEN, DMN, SRMA, 91191 Gif-sur-Yvette Cedex, France*
[b] *Mines ParisTech, Centre des Matériaux, CNRS UMR 7633, BP 87, 91003 Evry Cedex, France*

Abstract

A model is proposed to describe the mechanical behavior and the ductile failure at 25, 350 and 480 °C of Zircaloy–4 cladding tubes, as-received and hydrided up to 1200 wt. ppm (circumferential hydrides). The model is based on the Gurson–Tvergaard–Needleman model extended to account for plastic anisotropy and viscoplasticity. The model considers damage nucleation by both hydride cracking and debonding of the interface between the Laves phase precipitates and the matrix. The damage nucleation rate due to hydride cracking is directly deduced from quantitative microstructural observations. The other model parameters are identified from several experimental tests. Finite element simulations of axial tension, hoop tension, expansion due to compression and hoop plane strain tension experiments are performed to assess the model prediction capability. The calibrated model satisfactorily reproduces the effects of hydrogen and temperature on both the viscoplastic and the failure properties of the material. The results suggest that damage is anisotropic and influenced by the stress state for the non–hydrided or moderately hydrided material and becomes more isotropic for high hydrogen contents.

Key words: Zircaloy–4, hydrogen, plasticity, ductile fracture, model

*Corresponding author. Tel.: +33 1 69 08 12 28; Fax: +33 1 69 08 71 67.
Email addresses: matthieu.lesaux@cea.fr (M. Le Saux)

1. Introduction

Zirconium alloy fuel claddings are oxidized by the coolant water during normal operation in Pressurized Water Reactors (PWRs). A fraction of the hydrogen released is absorbed and diffuses into the cladding. The hydrogen is partly dissolved in the crystal lattice of zirconium but beyond the solubility limit of hydrogen in the metal, which is quite low (about 100 wt. ppm) at the cladding operating temperature (around 350 °C), the excess hydrogen atoms precipitate as hydride platelets. In Zircaloy–4 fuel cladding, hydrides are mainly oriented with their normal aligned along the tube radial direction (circumferential hydrides). Mean hydrogen contents up to 600 wt. ppm are observed in high burnup Zircaloy–4 cladding [1]. Higher hydrogen contents can be reached locally, due to thermal diffusion of hydrogen toward the colder outer surface of the cladding. These localized hydrogen–rich areas are called hydride rims or blisters. The risk of cladding failure during in–reactor transient events may be increased, due to the embrittling effect of hydrogen. For instance, during a Reactivity Initiated Accident (RIA), caused by the ejection of a control rod assembly in PWRs, the cladding tube would be submitted at the beginning of the transient to a fast (strain rate of about $1\,s^{-1}$) and biaxial mechanical loading (along cladding hoop and axial directions) due to Pellet–Clad Mechanical Interaction (PCMI) [2, 3]. During this early stage of the transient, cladding temperature quickly increases (heating rate of the order of $10^4\,°C.s^{-1}$) up to 600 °C on the tube inner surface while it remains around 350 °C on the outer surface [2]. Full–scale in–pile experiments performed in the NSRR or the CABRI reactors [4, 5] have shown that, in the case of Zircaloy–4 cladding, the fuel rod can withstand a lower level of deposited energy during the RIA transient when it has a very high burnup, due in particular to hydrogen–induced cladding embrittlement. The mechanical properties of the cladding material depend among other things on hydrogen content, temperature and stress/strain state [3, 6, 7, 8, 9].

Relevant failure models or criteria are needed for an accurate evaluation of the risk of cladding failure during in–reactor transients such as a RIA. Cladding

failure criteria used in transient fuel behavior codes for the PCMI stage are mostly expressed in terms of a critical strain [10] or a critical strain energy density [11, 12] or are based on a fracture mechanics approach [13]. These global (from a material point of view) criteria are usually established on the basis of separate–effect tests performed out–of–pile in laboratories. Their relevance depends on the representativeness of the mechanical tests with respect to the actual cladding thermal–mechanical loading and failure mode during a RIA. Most of the tests currently available reproduce only approximately these features [3, 8], which are quite difficult to generate out–of–pile, although some efforts were and are still made to manage it [8, 9, 14, 15, 16]. Generally, corrective factors are applied in order to take into account the differences in mechanical loading (biaxiality and strain rate in particular) between separate–effect tests and the actual conditions [12, 16]. However, it has been shown that the failure mode of the specimen depends on the type of test (specimen geometry, stress state, ...) and, often, is not fully representative of the PCMI–induced cladding failure [8]. Furthermore, the accurate interpretation of the test is sometimes tricky due for instance to the complex stress and strain fields generated.

Physically–based models, based on the local approach to fracture, may provide a better understanding of both the local material damage/failure mechanisms and the global specimens fracture modes, in order to justify or to improve the more global failure criteria used in fuel behavior codes. *A priori*, this kind of model is not limited to a particular sample geometry and a good transferability of laboratory test results to the larger and more complex actual component can be expected. Some of the most used models based on the continuum damage mechanics are those proposed by [17] and [18], based on a thermodynamical approach, and the model developed by [19], later modified by Tvergaard and Needleman [20, 21], initially based on a micromechanical approach. A micromechanical model, based on an extension of the void growth model of Rice and Tracey [22], was proposed in [23] to predict the ductile tearing of wrought alpha–annealed and beta–treated Zircaloy–2 and Zircaloy–4 without hydrogen. A model was developed in [24] to describe the mechanical behavior, including

damage, of Zircaloy–4 with hydrides of arbitrary orientation. The Zircaloy–4 matrix is modeled as an isotropic elastoplastic material and the hydrides are represented as elastic brittle inclusions with damage and preferred directions (*e.g.* circumferential and radial hydrides). The mechanical response of the material is derived from a stored potential strain-energy function. Unfortunately, the prediction capability of this model was illustrated on the basis of a very limited number of experimental data and the model is not yet able to predict the fracture of radial hydrides. A model based on the continuum damage mechanics, with a damage variable tuned for fresh (non–hydrided) Cold–Worked Stress Relieved (CWSR) Zircaloy–4 for temperatures of 25 and 350 °C, was recently proposed and applied to simulate the fracture of fuel claddings under PCMI loading during a RIA [25]. A Gurson–Tvergaard–Needleman (GTN) model with isotropic perfect plasticity was used in [26] to reproduce the mechanical behavior and the ductile failure of Zr–2.5Nb pressure tube material but it was anticipated that a better agreement with the experimental data would be obtained using more accurate model parameters and by taking into account strain hardening and anisotropy of elasticity and plasticity.

In this paper, a model based on the GTN model is proposed to describe the anisotropic viscoplastic mechanical behavior and the ductile fracture, at 25, 350 and 480 °C, of CWSR Zircaloy–4 tubes, as–received and hydrided (uniform distribution of circumferential hydrides across the tube thickness) up to 1200 wt. ppm. Some of the model parameters are directly related to measurable damage quantities (porosity, void nucleation rate, ...). This formalism was already successfully applied to represent the ductile fracture, at room temperature, of hydrided recrystallized Zircaloy–4 sheets [27]. The present model was adjusted by using the experimental data reported in a previous paper [8], which are summarized hereafter. Several types of tests, with various loading directions and stress/strain states, were performed with a mean strain rate of about $0.1\,s^{-1}$: Axial Tension (AT), Hoop Tension (HT), Expansion Due to Compression (EDC) and hoop Plane Strain Tension (PST). It was shown that the plasticity of the material is anisotropic. Plastic anisotropy depends on temperature but is not

significantly modified by hydrogen. The material mechanical strength decreases with increasing the temperature and the content of dissolved hydrogen and increases with increasing the precipitated hydride content. The material ductility increases with increasing temperature. A higher ductility is observed along the circumferential direction compared to the axial direction. At room temperature, the material is embrittled by hydrogen precipitated in the form of circumferential hydrides. At 350 °C and 480 °C, hydrogen, which is partially dissolved into the metal, does not have any significant effect on material ductility. A ductile fracture mode, involving void nucleation, growth and coalescence, was observed whatever the tested condition. In the non–hydrided material whatever the temperature and in the hydrided material tested at 350 °C and 480 °C, damage nucleation essentially occurs around Laves phase precipitates (within grains and at grain boundaries) and at grain boundary triple nodes. In the case of the hydrided material tested at room temperature, void nucleation is mainly caused by hydride cracking. Damage due to hydride cracking at room temperature occurs for a plastic strain higher than 0.08 and is faster with increasing hydrogen content. It is not significantly influenced by stress triaxiality in the studied range (from 1/3 to $1/\sqrt{3}$). No hydride cracking was observed at 350 °C and 480 °C.

The model proposed to reproduce these results is described in Section 2. Model parameters adjustment is presented in Section 3. In Section 4, the model is applied for finite element analysis of various mechanical tests.

2. Description of the model

2.1. Gurson–Tvegaard–Needleman potential

The potential of the Gurson–Tvergaard–Needleman model extended to anisotropic and viscoplastic behaviors is expressed as follows:

$$\Phi(\underline{\boldsymbol{\sigma}}, \sigma_\star, f_\star) = \left(\frac{\sigma_H}{\sigma_\star}\right)^2 + 2q_1 f_\star \cosh\left(q_2 \frac{3}{2}\frac{\sigma_m}{\sigma_\star}\right) - 1 - q_3 f_\star^2 \qquad (1)$$

where $\underline{\boldsymbol{\sigma}}$ is the macroscopic stress tensor, $\sigma_m = \sigma_{kk}/3$ is the macroscopic mean stress, $f_\star$ is the effective porosity and q_1, q_2 and q_3 are constant parameters

introduced on a phenomenological basis by Tvergaard and Needlemann [20, 21, 28] in order to take into account strain hardening and interaction between neighboring cavities. σ_H is the macroscopic Hill equivalent stress [29] used to represent plastic anisotropy:

$$\sigma_H = \sqrt{\underline{\boldsymbol{\sigma}} : \underline{\underline{\mathbf{H}}} : \underline{\boldsymbol{\sigma}}} \tag{2}$$

where $\underline{\underline{\mathbf{H}}}$ is a symmetric fourth rank tensor. When expressed in the anisotropy principal axes, which coincide with the tube reference system axes (radial direction r, circumferential direction θ and axial direction z), the equivalent stress is calculated as:

$$\sigma_H = \left[H_{rr}(\sigma_{\theta\theta} - \sigma_{zz})^2 + H_{\theta\theta}(\sigma_{zz} - \sigma_{rr})^2 + H_{zz}(\sigma_{rr} - \sigma_{\theta\theta})^2 + 2H_{r\theta}\sigma_{r\theta}^2 + 2H_{rz}\sigma_{rz}^2 + 2H_{\theta z}\sigma_{\theta z}^2\right]^{1/2} \tag{3}$$

This modification of the former GTN model only affects the contribution of deviatoric stresses. Damage remains isotropic. $\sigma_\star$ is the effective stress (in the matrix) of the porous material. It is implicitly defined by:

$$\Phi(\underline{\boldsymbol{\sigma}}, \sigma_\star, f_\star) = 0 \tag{4}$$

2.2. Damage description

The total porosity (having a mechanical effect), f_t, is expressed as a function of the porosity caused by the nucleation of new voids, f_n, and the porosity caused by the growth of existing voids by plastic deformation, f_g:

$$f_t = f_n + f_g \tag{5}$$

According to the observations detailed in [8], two state variables are used to describe void nucleation: f_{nL} corresponding to the nucleation of initially spherical voids by debonding of the interface between the Laves phase precipitates and the matrix and f_{nH} corresponding to the nucleation by hydride cracking of rectangular penny–shaped type voids or microcracks:

$$f_n = f_{nL} + f_{nH} \tag{6}$$

The GTN model is based on the analysis of a unit cell consisting of a single void, replacing randomly distributed voids, surrounded by a matrix subjected to periodic boundary conditions. Voids nucleated around Laves phase precipitates are randomly distributed but cracking of large hydrides results in the formation of groups of aligned voids. However , it is considered in a first approach that the potential effect of this non–uniform distribution of hydride–initiated voids on the overall mechanical properties can be neglected. Furthermore, it is important to keep in mind that the model proposed in this paper was tuned for Zircaloy–4 cladding tubes containing circumferential hydrides and loaded in tension along the hoop and axial directions. In other words, the model correctly describes the effect of hydrides when they are mostly parallel to the tensile direction(s) but it should not be applied in its current form when the tensile loading direction is perpendicular to the hydride platelets (*e.g.* a cladding tube with radial hydrides submitted to tension along the hoop and/or the axial directions or a cladding with circumferential hydrides loaded in tension along the radial direction) since it well-known that the embrittlement due to the presence of hydrides is more important in this last configuration [30].

Gologanu et al. [31] proposed an extension of the GTN model to materials containing ellipsoidal voids and showed that the effect of a crack on damage is equivalent to the effect of a void having the same projected area. Then, the microcracks generated by hydride cracking are assumed to have the same mechanical effect than cylindrical voids with the same projected area within the plane perpendicular to the principal loading direction (Fig. 1). Contrary to the nucleation of voids created by debonding (after debonding, the particle inside the void is not expected to have a mechanical contribution anymore), the nucleation of microcracks does not induce a variation of porosity. Therefore, although its mechanical effect is well taken into account through the expression of the effective nucleation porosity f_n (Eq. 6), the fictional volume due to the nucleation of microcracks by hydride cracking must not be included into the

actual porosity (associated with a volume variation), which is then given by:

$$f = f_{nL} + f_g \tag{7}$$

A similar approach was used in [27], [32] and [33]. The void growth rate is governed by mass conservation (it is assumed that porosity is not modified by an elastic volume variation):

$$\dot{f}_g = (1-f)\mathrm{tr}(\underline{\dot{\boldsymbol{\epsilon}}}^p) = (1-f)^2 \dot{p}\underline{\mathbf{n}} : \underline{\mathbf{I}} \tag{8}$$

where $\underline{\mathbf{n}}$ is the flow direction and $\underline{\mathbf{I}}$ is the second order unit tensor. In order to account for the acceleration of void growth during void coalescence, the effective porosity, expressed here as a function of the total porosity f_t, is described as follows [20]:

$$f_\star(f_t) = \begin{cases} f_t & \text{if } f_t < f_c \\ f_c + \delta(f_t - f_c) & \text{otherwise} \end{cases} \tag{9}$$

where f_c is the critical porosity at which void coalescence begins (so that the porosity is more damaging than if it remained spherical) and δ is a phenomenological factor introduced to artificially accelerate void growth:

$$\delta = \frac{f_{\star u} - f_c}{f_f - f_c} > 1 \tag{10}$$

Failure occurs when $f_\star = f_{\star u} = 1/q_1$, *i.e.* when $f_t = f_f = f_c + (f_{\star u} - f_c)/\delta$. For the sake of simplification, the model does not explicitly describe, as done for example by [34] or [35], the acceleration (by a void sheet mechanism) of the coalescence of primary voids (created by hydride cracking) due to the presence of secondary voids (resulting from the debonding of the matrix around the Laves phases) within the shear bands between them. However, this acceleration can be implicitly reproduced through the f_c and δ parameters.

2.3. Viscoplastic flow

The viscoplastic flow potential is expressed as follows:

$$\Omega = \sigma_\star \geq 0 \tag{11}$$

The viscoplastic strain rate tensor is obtained by assuming the normality rule:

$$\underline{\dot{\boldsymbol{\epsilon}}}^p = (1-f)\dot{\lambda}\frac{\partial\Omega}{\partial\underline{\boldsymbol{\sigma}}} = (1-f)\dot{\lambda}\frac{\partial\sigma_\star}{\partial\underline{\boldsymbol{\sigma}}} \tag{12}$$

where $\dot{\lambda}$ is the plastic multiplier given by the viscoplastic flow law of the material, F_{vp} :

$$\dot{\lambda} = F_{vp}(\Omega) \tag{13}$$

$\sigma_\star$ is an homogeneous differentiable function of degree 1 of $\underline{\boldsymbol{\sigma}}$. According to the Euler theorem, $(\partial\sigma_\star/\partial\underline{\boldsymbol{\sigma}}) : \underline{\boldsymbol{\sigma}} = \sigma_\star$. Then Eq. 12 gives:

$$\underline{\dot{\boldsymbol{\epsilon}}}^p : \underline{\boldsymbol{\sigma}} = (1-f)\dot{\lambda}\frac{\partial\sigma_\star}{\partial\underline{\boldsymbol{\sigma}}} : \underline{\boldsymbol{\sigma}} = (1-f)\dot{\lambda}\sigma_\star \tag{14}$$

By enforcing equality between microscopic plastic dissipation and macroscopic plastic work:

$$\underline{\dot{\boldsymbol{\epsilon}}}^p : \underline{\boldsymbol{\sigma}} = (1-f)\dot{p}\sigma_\star \tag{15}$$

the evolution of the accumulated viscoplastic strain p is obtained by comparison with Eq. 14:

$$\dot{p} = \dot{\lambda} = F_{vp}(\Omega) \tag{16}$$

The viscoplastic strain tensor is then given by:

$$\underline{\dot{\boldsymbol{\epsilon}}}^p = (1-f)\dot{p}\underline{\mathbf{n}} \text{ with } \underline{\mathbf{n}} = \frac{\partial\sigma_\star}{\partial\underline{\boldsymbol{\sigma}}} \tag{17}$$

$\sigma_\star$ being implicitly defined, the flow direction $\underline{\mathbf{n}}$ can be calculated by noting that for a given porosity a variation of $\underline{\boldsymbol{\sigma}}$ induces a variation of $\sigma_\star$ so that Φ remains equal to zero:

$$\delta\Phi = \frac{\partial\Phi}{\partial\underline{\boldsymbol{\sigma}}} : \delta\underline{\boldsymbol{\sigma}} + \frac{\partial\Phi}{\partial\sigma_\star}\delta\sigma_\star = 0 \tag{18}$$

Then:

$$\underline{\mathbf{n}} = -\left(\frac{\partial\Phi}{\partial\sigma_\star}\right)^{-1}\frac{\partial\Phi}{\partial\underline{\boldsymbol{\sigma}}} \tag{19}$$

with

$$\frac{\partial\Phi}{\partial\sigma_\star} = -\frac{2\sigma_H^2}{\sigma_\star^3} - \frac{3f_\star q_1 q_2\sigma_m}{\sigma_\star^2}\sinh\left(q_2\frac{3}{2}\frac{\sigma_m}{\sigma_\star}\right) \tag{20}$$

and

$$\frac{\partial\Phi}{\partial\underline{\boldsymbol{\sigma}}} = \frac{2}{\sigma_\star^2}\underline{\underline{\mathbf{H}}} : \underline{\boldsymbol{\sigma}} + \frac{f_\star q_1 q_2}{\sigma_\star}\sinh\left(q_2\frac{3}{2}\frac{\sigma_m}{\sigma_\star}\right)\underline{\mathbf{I}} \tag{21}$$

3. Identification of the model parameters

3.1. Methodology

Nine parameters of the model have to be determined: the viscoplastic flow law F_{vp}, the Hill tensor $\underline{\underline{\mathbf{H}}}$, the nucleation laws respectively related to Laves phase precipitates $\dot{f}_{nL}$ and to hydrides $\dot{f}_{nH}$, the q_1, q_2 and q_3 parameters, the critical porosity leading to void coalescence f_c and the acceleration parameter δ. Experimental results given in [8] were used to adjust these parameters and to evaluate the prediction capability of the model.

The model was implemented into the finite element code Cast3M developed at CEA (`http://www-cast3m.cea.fr/`) by using the UMAT (User MATerial) subroutine. A fourth order Runge–Kutta method with an adaptive step size control was used to integrate the model internal variables. Due to numerical difficulties (equilibrium of the whole structure) appearing when the material at one or a few Gauss points is broken (*i.e.* when the critical value for damage has been reached), it has not been possible to simulate with Cast3M the whole fracture process of the specimens tested by [8]. Therefore, the study has been focused on the prediction of crack initiation. Since crack propagation was not fully simulated, symmetries of the investigated systems (AT, HT, EDC and PST tests) were used, allowing a sufficiently small mesh size while keeping reasonable computation times. Quadratic elements were used, with reduced integration so that all Gauss points of a given element had the same volume and high pressure variations inside the elements were avoided. Meshes and limit conditions used to simulate the various tests reported in [8] are described in Section 4.

Since no damage was observed before plastic instability [8], the identification of F_{vp} and $\underline{\underline{\mathbf{H}}}$ was made on the basis of experimental data obtained before necking. q_1, q_2, q_3 and δ were fixed to values commonly used in the literature. $\dot{f}_{nH}$ was directly deduced from the measured damage kinetics reported in [8]. $\dot{f}_{nL}$ and f_c were determined in order to obtain a good agreement between local strains calculated by Finite Element Analysis (FEA) at crack initiation (failure reached at one Gauss point) and local strains experimentally measured after

specimen failure. It was considered that, except for HT tests performed on the non–hydrided material or on the hydrided material at 350 °C and 480 °C, crack initiation leads nearly instantaneously to final fracture of the sample (crack propagation is unstable):

- In the case of AT (Axial Tension) specimens, finite element simulations and strain measurements by Digital Image Correlation (DIC) have shown that, for a sufficient strain level, two narrow localized plastic strain bands, symmetric with respect to the specimen axis, appear inside the diffuse neck. These bands are inclined at about 56° to the tensile axis. For the non–hydrided material whatever the temperature or the hydrided material tested at 350 °C and 480 °C, fracture initiates at the junction of these bands and propagates along one of them [8]. Once these bands have developed, the material on both sides of the bands does not deform anymore and the specimen width variation becomes negligible. Fracture of the hydrided specimens tested at room temperature occurs suddenly before the formation of these bands, perpendicularly to the tensile direction. In that case, specimen deformation between crack initiation and final fracture is very small. Then it was considered that, whatever the conditions tested by [8], AT specimen width variation at crack initiation is very close to the width reduction of the broken specimen.

- On the one hand, in the case of HT (Hoop Tension) tests performed whatever the temperature on the material non–hydrided or hydrided at 400 wt. ppm or at 350 °C and 480 °C on the hydrided material, the crack initiated at the center of the specimen gauge propagates in a relatively stable manner along the specimen width [8]. Specimens width contraction continues after initiation of the central crack, until final fracture. Therefore, the strain profile is very different at crack initiation and at fracture. On the other hand, these profiles are probably close in the case of the HT hydrided specimens tested at room temperature, which fail suddenly perpendicularly to the loading direction.

- Failure of non–hydrided EDC (Expansion Due to Compression) specimens occurs by through–thickness crack propagation along a plane inclined at 45° from the principal loading direction [8]. The hydrided material tested at room temperature fails along a macroscopic plane orthogonal to the principal loading direction. In both cases, the specimen outer diameter does not significantly evolve between crack initiation and final fracture.

- Macroscopic failure modes of PST (Plain Strain Tension) specimens are close to those of EDC specimens [8] and it is expected that local strains of PST specimens at crack initiation and at failure are not very different.

Predictions of the model were thus evaluated on the basis of width reduction profiles for AT and HT tests, variation of the outer diameter for EDC tests and hoop strain at the outer surface for PST tests. Although plastic anisotropy, which affects void growth, is taken into account, it has not been possible to determine a single set of parameters making it possible to accurately simulate all the tests. This can be attributed to an anisotropy of damage, which is not accounted for in the model. Nevertheless, in order to improve the knowledge of material damage and specimens failure, a first set of parameters was determined on the basis of AT tests only. Then these parameters were used to simulate the other tests.

3.2. Plastic anisotropy

For the determination of $\underline{\underline{\mathbf{H}}}$, the axial direction was fixed as the reference one, leading to $\sigma_H = \sigma_{zz}$ for an AT test (normalization condition). As shown in [8], plastic anisotropy depends on temperature and is independent on hydrogen content up to 1200 wt. ppm (circumferential hydrides). The Hill coefficients previously identified in [36], with a dependence on temperature, are used in the present work. The good agreement with the experimental data reported in [8] is verified in Fig. 2.

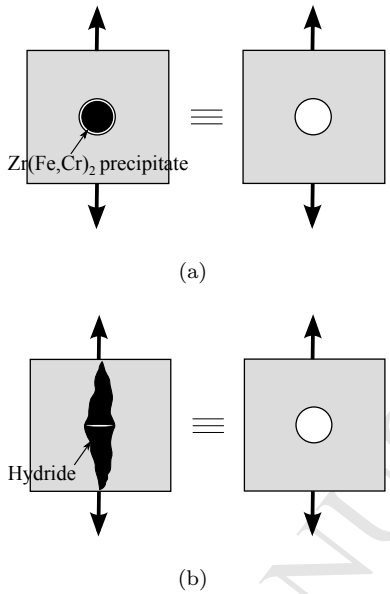

Figure 1: Void nucleation by (a) debonding of the interface between the Laves phase precipitates and the matrix and (b) hydride cracking.

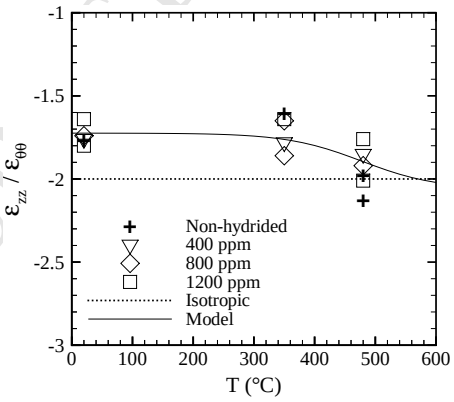

Figure 2: Experimental and calculated evolutions as a function of temperature for various hydrogen contents of the ratio of axial to hoop plastic strains measured during AT tests.

3.3. Viscoplastic flow of the undamaged material

A multiplicative non–linear isotropic hardening model is used to describe the viscoplastic flow of the undamaged material, F_{vp}. The equivalent viscoplastic strain rate is given by:

$$\dot{p} = \dot{p}_0 \left(\frac{\sigma_H(T)}{\eta(p, T, C_{Hs}, C_{Hp})} \right)^{1/m(T)} \tag{22}$$

where m is the strain rate sensitivity coefficient, $\dot{p}_0$ is the reference strain rate fixed to $1\,\mathrm{s}^{-1}$. η is a non–linear viscosity coefficient which can be expressed as:

$$\eta(p, T, C_{Hs}, C_{Hp}) = K(T, C_{Hs}, C_{Hp}) L(p, T, C_{Hp}) \tag{23}$$

where K is the strength coefficient and L is the strain hardening coefficient depending on p. Note that the instantaneous strain hardening exponent is given by $n = \partial \ln L / \partial \ln \epsilon^p$ in the case of a uniaxial loading. According to the experimental results [8], the strength coefficient K depends on temperature T, hydrogen in solid solution content C_{Hs} and precipitated hydride content C_{Hp}. The influence of hydrides on K decreases when temperature increases, as mechanical properties of hydrides evolve with temperature. The strain hardening coefficient L is expressed as a function of plastic strain, temperature and hydride content. Tests reported in [8] were performed under only one strain rate ($0.1\,\mathrm{s}^{-1}$). Therefore, the value proposed in [36] for m is used to describe the temperature dependent strain rate sensitivity of the material, which is assumed to be independent on hydrogen content according to [37]. Dissolved and precipitated hydrogen contents are evaluated from the total hydrogen content C_H and the terminal solubility limit of hydrogen C_s:

$$C_{Hs}(T) = \min(C_H; C_s(T)); \; C_{Hp}(T) = C_H - C_{Hs}(T) \tag{24}$$

According to [38], the terminal solubility limit of hydrogen in Zircaloy–4 under equilibrium conditions up to 550 °C is given by $C_s(T) = 99000 \exp(-34523/RT)$, where $R = 8.314\,\mathrm{J.mol^{-1}.K^{-1}}$ is the gas constant.

Since no damage was experimentally observed before the onset of necking [8], the viscoplastic flow law was adjusted without taking into account any

coupling with damage. Moreover, isothermal conditions are assumed since the adiabatic heating due to plastic dissipation is not expected to be significant for the conditions tested in [8], according to the results discussed in [39]. While considering the normalization condition chosen for the determination of Hill coefficients, the model parameters K and L were identified using only AT test results. A least squares fitting method, based on AT stress–plastic strain data before necking, was used. Values of the adjusted parameters are reported in Table 1.

As shown in Fig. 3, the model accurately reproduces the plastic properties of the material up to uniform elongation. In particular, the combined effects of temperature and hydrogen content on strength and strain hardening are correctly described.

3.4. Void nucleation

3.4.1. Debonding between the Laves phase precipitates and the matrix

Void nucleation by debonding of the interface between Laves phase precipitates and the matrix is considered to be controlled by plastic strain:

$$\dot{f}_{nL} = A_{nL}\dot{p} \tag{25}$$

It is difficult to quantify experimentally the nucleation kinetics of these voids because of the small size of the precipitates. Then the following nucleation law is used:

$$A_{nL} = \begin{cases} \frac{f_{NL}}{p_{NLf} - p_{NLi}} & \text{if } p_{NLi} < p < p_{NLf} \\ 0 & \text{otherwise} \end{cases} \tag{26}$$

where p_{NLi} is the minimum plastic strain at which nucleation starts and p_{NLf} is the maximum plastic strain at which nucleation stops. f_{NL} is the volume fraction of Laves phase precipitates around which void nucleation can occur. Iron and chromium are nearly insoluble in the α phase of zirconium up to 800 °C [40]. By considering that all iron and chromium atoms precipitate in the form of Laves phases $Zr(Fe,Cr)_2$, the precipitates volume fraction can be evaluated from the chemical composition of the material (1.3 wt.% Sn, 0.21 wt.%

Table 1: Model parameters relative to plastic anisotropy and viscoplasticity (T in K, C_{Hs} and C_{Hp} in wt. ppm).

Elasticity [36]:

$E = 1.059 \cdot 10^{11} - 36 \cdot 10^{6} T$, $\nu = 0.342$

Strain rate sensitivity [36]:

$m = 1/[77.68 M_T + 4.11(1 - M_T)]$

where $M_T = 1/[1 + \exp(10.2(T/692 - 1))]$

Strain hardening:

$L = (p + 1 \cdot 10^{-4})^{n_0} \exp(-\alpha_n p) + (1 - \exp(-\alpha_n p))$

with $n_0 = (1 + 1.45 \cdot 10^{-4} C_{Hp})[4.86 \cdot 10^{-2} N_{0T} + 2.35 \cdot 10^{-2}(1 - N_{0T})]$

where $N_{0T} = 1/[1 + \exp(12(T/(810 - 9.19 \cdot 10^{-2} C_{Hp}) - 1))]$

and $\alpha_n = (53.16 + 1.27 \cdot 10^{-2} C_{Hp})[1 + \exp(11.1(T/738 - 1))]$

Strength:

$K = [1 - 1.175 \cdot 10^{-4} C_{Hs} + (6.15 \cdot 10^{-5} - 4.38 \cdot 10^{-8} T) C_{Hp}][(1.409 \cdot 10^{9} - 8.952 \cdot 10^{5} T) K_T + 4.05 \cdot 10^{7}(1 - K_T)]$

where $K_T = 1/[1 + \exp(1.77(T/1007 - 1))]$

Plastic anisotropy [36]:

$H_{rr} = 0.485 + 9.5 \cdot 10^{-2}/[1 + \exp(12(T/740 - 1))]$

$H_{\theta\theta} = 1 - H_{rr}$

$H_{zz} = 0.52 + (-0.23 + 4 \cdot 10^{-4} T)/[1 + \exp(15(T/550 - 1))]$

$H_{r\theta} = H_{rz} = H_{\theta z} = 1.5$

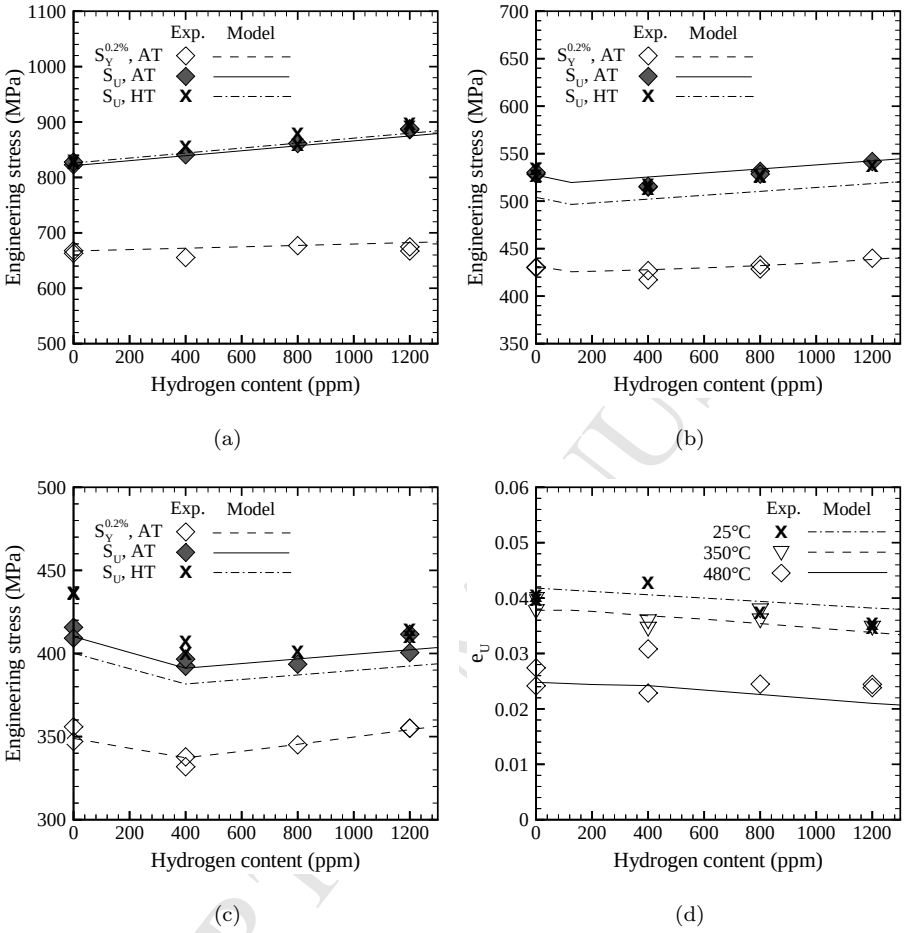

Figure 3: Experimental and calculated evolutions as a function of hydrogen content of the yield stress at 0.2% plastic strain $S_Y^{0.2\%}$ for AT tests and the ultimate (or maximum) stress S_U for AT and HT tests performed at (a) 25 °C, (b) 350 °C and (c) 480 °C. (d) Experimental and calculated variations of the uniform elongation at the onset of necking (plastic strain corresponding to S_U) e_U as a function of hydrogen content for AT tests conducted at 25 °C, 350 °C and 480 °C.

Fe, 0.11 wt.% Cr, 0.128 wt.% O, Zr balance): $f_L = 0.0045$. A similar value was found by [41]. It has been observed that Laves phase precipitates are preferential sites for the nucleation of damage in the non–hydrided material whatever the temperature and in the hydrided material tested at 350 °C and 480 °C. It is assumed that all $Zr(Fe,Cr)_2$ precipitates are likely to contribute to void nucleation so that $f_{NL} = f_L = 0.0045$. This is a strong assumption, quite difficult to verify experimentally and then made for lack of more precise information, but it appears that this assumption is reasonable since, as it will be shown, the model describes quite well the failure of the material.

Values of 0.04 and 0.3 were respectively found by inverse analysis for p_{NLi} and p_{NLf} for AT tests, whatever the temperature. Therefore, void nucleation by debonding of the interface between the matrix and Laves phase precipitates starts at the onset of necking within the specimen.

3.4.2. Hydride cracking

According to experimental observations [8], void nucleation by hydride cracking at room temperature is controlled by plastic strain of the matrix:

$$\dot{f}_{nH} = A_{nH}\dot{p} \tag{27}$$

Hydrides fail only when they are submitted to a tensile loading. Thus the previous equation applies only if $\sigma_{kk} > 0$. Otherwise, $\dot{f}_{nH} = 0$. Damage nucleation kinetics due to hydride cracking was quantified in [8] as a function of plastic strain by counting the number of voids on thickness–length cross–sections of specimens failed at room temperature. The crack density N_H was measured at different distances from the specimen fracture surface and related to the measured local plastic strain. According to experimental observations [8], damage is considered to be homogeneous across the specimen width so that the damage observed in the thickness–length plane is representative of the specimen damage. The microcracks resulting from hydride cracking under uniaxial tension appear as elongated rectangles in the plane perpendicular to the loading direction (width d_H and length l_H along the specimen thickness and

width, respectively). It is assumed that all microcracks have initially the same width d_H, taken equal to the mean value of microcracks width measured in [8] (*i.e.* 0.4 μm), which is obviously close to the mean thickness of hydrides. These microcracks are supposed to have the same mechanical effect than cylindrical–shaped voids with the same projected area $d_H l_H$ (Fig. 1) [27]. Then, the nucleation porosity can be evaluated from the crack density N_H measured by [8]:

$$f_{nH} = \frac{\pi d_H^2 N_H}{4} \tag{28}$$

Fig. 4 shows the evolution of the nucleation porosity as a function of the equivalent plastic strain.

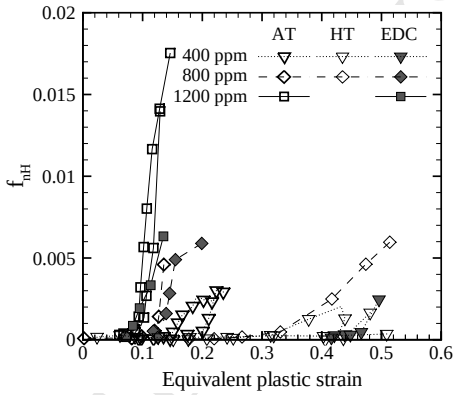

Figure 4: Nucleation porosity due to hydride cracking as a function of equivalent plastic strain for AT, HT and EDC tests performed at room temperature on the material containing various hydrogen contents.

The void nucleation rate is obtained by deriving Eq. 28. The void nucleation intensity is then given by:

$$A_{nH} = \frac{\pi d_H^2}{4} \frac{dN_H}{dp} \tag{29}$$

Nucleation kinetics by hydride cracking at room temperature are not exactly the same under axial tension and hoop tension. The model in its current form does not take this anisotropy of damage into account. However, in a first approach, A_{nH} is adjusted by using only AT tests results (this arbitrary choice was made because there were a little bit more data available for this type of test). The

normal law proposed in [42] is retained :

$$A_{nH} = \frac{f_{NH}}{s_{NH}\sqrt{2\pi}} \exp\left(-\frac{1}{2}\left(\frac{p-\epsilon_{NH}}{s_{NH}}\right)^2\right) \tag{30}$$

where f_{NH} is the volume fraction of hydrides that can contribute to void nucleation, $\epsilon_{NH} = 0.331 - 1.41 \cdot 10^{-4} C_{Hp}$ is the average nucleation strain and $s_{NH} = 5.97 \cdot 10^{-2} - 2.25 \cdot 10^{-5} C_{Hp}$ is the standard deviation of the failure strains distribution. The volume fraction of hydrides can be expressed as a function of the total precipitated hydrogen content C_{Hp} (in wt. ppm): $f_{ZrH} = 6.7 \cdot 10^{-5} C_{Hp}$. Eq. 24 is used to obtain C_{Hp} from the total hydrogen content and the temperature. According to the observations made by [8], hydrides do not fail at 350 °C and 480 °C. The volume fraction of hydrides that are likely to break thus depends on temperature. According to [43], [44], [45] and [46], the embrittling effect of hydrides decreases beyond about 100 °C and becomes negligible around 300 °C. On the basis of these results, f_{NH} is expressed as a function of f_{ZrH} and T (in K) so that $f_{NH} = f_{ZrH}$ at room temperature and $f_{NH} = 0$ above about 300 °C: $f_{NH} = f_{ZrH}/[1 + \exp(18(T/450 - 1))]$. This transition law as a function of T is approximate since, actually, it may depend on the material, the morphology of hydrides and the type of test.

3.5. Void coalescence

The values of q_1, q_2 and q_3 parameters, introduced to account for interactions between neighboring voids, are generally obtained on the basis of unit cell calculations describing one type of interaction. Here, values commonly used in the literature are chosen: $q_1 = 1.5$, $q_2 = 1$ and $q_3 = q_1^2$. The effective porosity to fracture then equals $f_{\star u} = 1/q_1 \approx 0.67$.

The function $f_\star$ (Eq. 9) includes two adjustable parameters: f_c and δ. Most of the load–displacement curves measured by [8] do not show any significant crack propagation slope before final failure and, as already mentioned, it has not been possible to simulate crack propagation for these tests. Therefore, δ was arbitrary fixed to 5 whatever the temperature and the hydrogen content, knowing that values reported in the literature are generally comprised between 3

and 8. The critical porosity leading to void coalescence cannot be reliably determined from the metallurgical observations reported in [8]. f_c was thus evaluated by inverse analysis on the basis of mechanical testing results. It was considered that f_c does not depend on stress and strain triaxiality. The identification gives $f_c = 0.0045$ in the absence of hydride cracking (non–hydrided material or hydrided material tested at 350 °C and 480 °C). Void coalescence thus occurs for a porosity equal to the volume fraction of Laves phase precipitates around which voids can nucleate (f_{NL}). The low strain hardening of the material may explain this low value of f_c. For all investigated levels of hydrogen, a value of 0.03 was found for f_c when void nucleation mainly occurs by hydride cracking at room temperature. This value is close to the maximum nucleation porosity measured for the material hydrided at 1200 wt. ppm (Fig. 4). Therefore, in the highly hydrided material, void growth is limited before coalescence and failure is mainly controlled by hydride cracking. In order to take into account the effects of hydrogen content and temperature on the main damage mechanism (hydride cracking or debonding of the interface between Laves phase precipitates and the matrix), the critical porosity leading to void coalescence is expressed as follows, using the temperature dependency adjusted for f_{NH} for the critical porosity associated to hydride cracking: $f_c = \max(0.0045; 0.03/[1 + \exp(18(T/450 - 1))])$.

f_c is higher when void nucleation mainly results from hydride cracking than when it occurs by debonding of the matrix/Laves phase precipitates interface (but the void nucleation kinetics is faster when it is due to hydride cracking). This is in accordance with the results reported by [47] showing that the higher the initial porosity the higher the porosity for which coalescence occurs. Indeed, volume fraction of hydrides likely to contribute to void nucleation, f_{NH}, is greater than volume fraction of Laves phase precipitates around which void nucleation can occur, f_{NL}. Finally, the porosity at failure, $f_f = f_c + (f_{\star u} - f_c)/\delta$, equals 0.137 in the absence of hydride cracking and 0.157 when void nucleation essentially occurs by hydride cracking at room temperature.

3.6. Mesh size

Finite element calculations performed with models based on a local approach are mesh size dependent due to the material softening resulting from damage. Mesh size can be related to metallurgical parameters such as grain size or distance between inclusions [18, 48] but the most common approach to solve this problem consists in considering mesh size as an adjustable parameter. A mesh size of $50\times50\,\mu$m was determined by [37] for recrystallized Zircaloy–4, hydrided or not, tested at room temperature. In order to have a satisfactory description of local mechanical fields while keeping reasonable computation times, a mesh size of $100\times100\times100\,\mu$m ($100\times100\,\mu$m in 2D) is chosen here, whatever the temperature and the hydrogen content. This mesh size is assimilated to a material parameter (characteristic length) and should be similar for all calculations. Calculations were performed for some of the tested conditions with the model presented in the present paper with mesh sizes of 75, 100 and 200 μm. The results have shown that the initiation of failure occurs a little bit sooner in the case of the finer mesh but the difference is not very large. A larger sensitivity to mesh size is expected for the stage of crack propagation but the simulation of this last stage is not the main issue of the present study, more focused on the prediction of crack initiation. Adjusted values of model parameters are given in Table 2.

4. Application of the model: finite element simulations

4.1. Axial tensile test

Only one eighth of the specimen is meshed. Standard symmetry conditions are applied. The displacement is applied to the pin passing through the cladding and the bored end–cap. As shown in Fig. 5, stress–plastic strain curves are well reproduced by the calculations up to a global plastic strain level of about 0.08. The effects of temperature and hydrogen content are correctly taken into account. Simulations over-predict the global plastic strain (deduced from the cross–end displacement) at failure.

Table 2: GTN model parameters adjusted on the basis of AT tests; for some parameters, values identified from HT and EDC tests results are written within brackets (T in K et C_{Hp} in wt. ppm).

Elasticity, behavior of the undamaged material, anisotropy:

see Table 1

Void nucleation:

$$A_{nL} = \begin{cases} \frac{f_{NL}}{p_{NLf} - p_{NLi}} & \text{if } p_{NLi} < p < p_{NLf} \\ 0 & \text{otherwise} \end{cases}$$

where $f_{NL} = 0.0045$

$p_{NLi} = 0.04$ (0.2 for hoop tension)

$p_{NLf} = 0.3$ (1 for hoop tension)

$$A_{nH} = \frac{f_{NH}}{s_{NH}\sqrt{2\pi}} \exp\left(-\frac{1}{2}\left(\frac{p - \epsilon_{NH}}{s_{NH}}\right)^2\right)$$

where $f_{NH} = 6.7 \cdot 10^{-5} C_{Hp} / [1 + \exp(18(T/450 - 1))]$

$\epsilon_{NH} = 0.331 - 1.41 \cdot 10^{-4} C_{Hp}$

(0.544 for hoop tension for the material hydrided at 400 wt. ppm)

$s_{NH} = 5.97 \cdot 10^{-2} - 2.25 \cdot 10^{-5} C_{Hp}$

Void coalescence:

$q_1 = 1.5$, $q_2 = 1$, $q_3 = q_1^2$

$f_c = \max(0.0045; 0.03/[1 + \exp(18(T/450 - 1))])$

$\delta = 5$

Mesh size:

$100 \times 100 \times 100\,\mu$m in 3D, $100 \times 100\,\mu$m in 2D

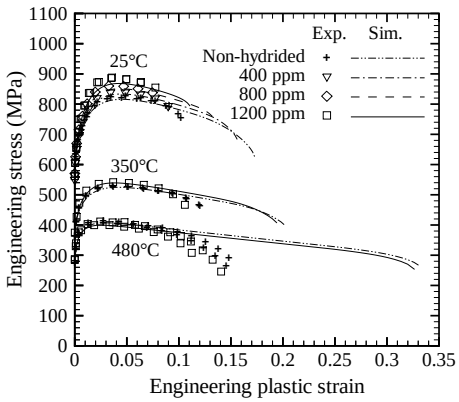

Figure 5: Experimental and calculated engineering stress–plastic strain curves for AT tests, for various temperatures and hydrogen contents.

However, width reductions at failure are correctly predicted (Fig. 6). Width reductions calculated at the global plastic strain at which failure is expected to occur according to experimental stress–plastic strain curves are lower than experimentally measured width reductions. This suggest that, due to the significant elastic energy accumulated into the tensile machine (with a relatively low stiffness) and the specimen (with an important length), AT tests take place in a quite unstable manner so that the measured load–displacement curves do not include the whole response of the specimen after necking. Besides, the later strain localization predicted by the simulations may be partly due to the fact that the description of necking, which is very sensitive to strain hardening and strain rate sensitivity, is not perfect and that the viscoplastic flow law used does not have a stress threshold. The excessively high strain level calculated at 480 °C far away from the fracture surface (Fig. 6(a)) is consistent with these assumptions. These observations confirm that the adjustment of the parameters of the model has to be based on local strain measurements rather than on global stress–plastic strain curves.

The calculations satisfactorily reproduce the hydride–induced embrittlement at room temperature, the negligible effect of hydrogen at 350 °C and 480 °C and the increase in material ductility with increasing temperature. The model pa-

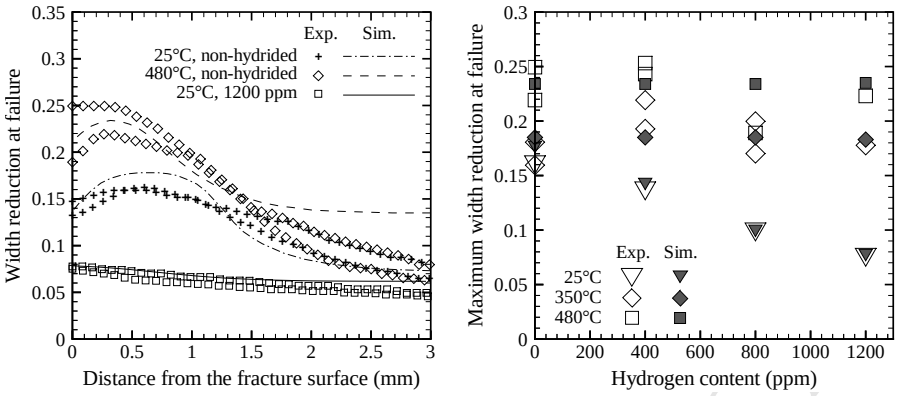

(a) (b)

Figure 6: Experimental and calculated width reductions at failure of AT specimens: (a) profiles with respect to the fracture surfaces, (b) maximum values.

rameters that describe the damage associated with Laves phase precipitates do not depend on temperature. Therefore, the increase in ductility when increasing the temperature is due to the stabilizing effect on strain localization of material viscosity, which increases with increasing temperature. As illustrated in Fig. 7, experimental (measured by DIC) and calculated strain fields before failure of AT specimens are in good agreement.

In the case of the non–hydrided material whatever the temperature and the hydrided material tested at 350 °C and 480 °C, damage at crack initiation is essentially localized at the center of the neck (Fig. 8), where stress and strain triaxiality and thus void growth are maximum under the effect of localized necking. Calculations show that damage of the hydrided material tested at room temperature is more diffuse and mostly controlled by void nucleation. In that case, the material fails before void growth becomes significant. The higher the hydrogen content the more limited the void growth.

Whatever the conditions tested by [8], failure of AT specimens initiates at about 3–4 mm from the specimen mid–length plane. This location of crack initiation is correctly predicted by the simulations. Deformation of the specimen

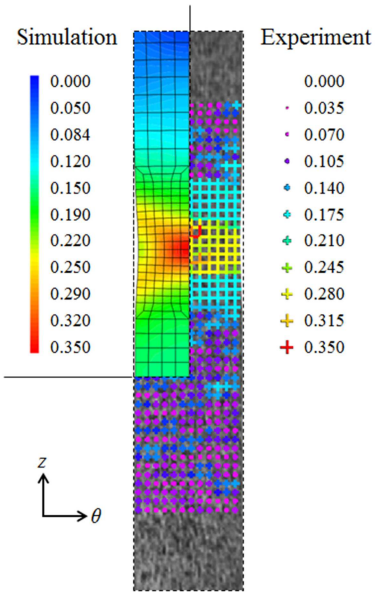

Figure 7: Green–Lagrange axial strain fields calculated by FEA and measured by DIC for a maximum width variation of −0.13 at the outer surface of a non–hydrided AT specimen tested at room temperature.

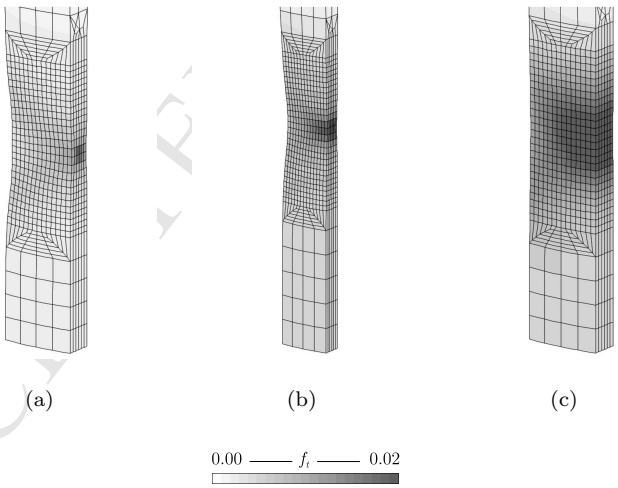

Figure 8: Total porosity fields calculated at crack initiation of AT specimens: (a) 25 °C, non–hydrided material, (b) 480 °C, non–hydrided material, (c) 25 °C, material hydrided at 1200 wt. ppm.

is maximum at the ends of gauge lengths at the beginning of the test. These heterogeneities move towards the mid–plane of the gauge lengths during loading. Necking and then failure occur near these heterogeneities before these last reach the mid–plane of the gauge lengths. Strain and porosity fields calculated at crack initiation suggest that the orientation of the macroscopic plane of failure (56° or 90° to the main loading direction, depending on the condition) could have been reproduced with a fitted mesh if crack propagation could have been simulated.

4.2. Hoop tensile test

According to symmetries, only one eighth of the system is considered. Standard boundary conditions are applied and a contact area involving sliding with friction (Coulomb's friction law with a coefficient of 0.4 [36]) is defined between the inner surface of the ring specimen and the outer surface of the D–shaped die insert. The cross-head displacement is applied on the mid–length plane of the sample.

As shown in Fig. 9, stress–plastic strain curves are not perfectly reproduced by the calculations for low global plastic strain levels. This deviation, which is not observed in the case of AT tests (Fig. 5), is attributed to a perfectible description of strain hardening along the hoop direction: kinematic strain hardening is not taken into account and model parameters describing strain hardening were adjusted only on AT tests results. Kinematic strain hardening can induce slightly faster void growth and strain localization than isotropic strain hardening [33] but it is considered that local strains at failure are not significantly modified.

Whatever the tested conditions, failure initiates according to the experiments at the inner surface of the sample at the middle of its gauge length, where plastic strain and triaxiality are the highest (Fig. 10).

Except for the material hydrided at 1200 wt. ppm tested at room temperature, strains at failure of HT specimens are under–estimated by the calculations (Figs. 9 and 11) performed by using the model with parameters identified in a first approach on the results obtained under axial tension only. As already

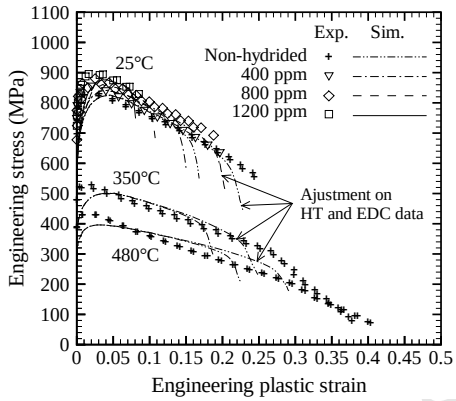

Figure 9: Experimental and calculated engineering stress–plastic strain curves for HT tests, for various temperatures and hydrogen contents. Results of calculations performed with parameters adjusted on HT and EDC tests data are included.

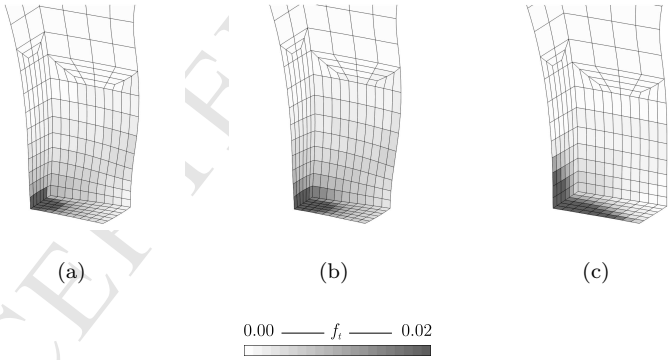

Figure 10: Total porosity fields calculated at crack initiation of HT specimens: (a) 25 °C, non–hydrided material, (b) 480 °C, non–hydrided material, (c) 25 °C, material hydrided at 1200 wt. ppm.

mentioned in Section 3, it has not been possible to correctly simulate both AT tests and HT tests with a single set of parameters. Therefore, the difference in ductilities measured during AT tests and HT tests [8] cannot be fully explained by the difference of deformation and failure modes of the two types of specimens. In particular, finite element calculations show that the higher ductility of HT specimens by comparison to AT specimens is not due to a delayed plastic strain localization.

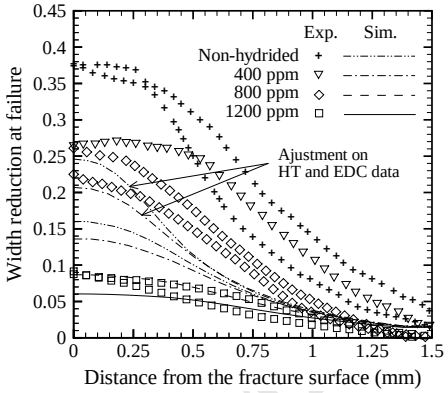

Figure 11: Experimental and calculated profiles of width reduction at failure with respect to the fracture surface of HT specimens tested at room temperature. Results of calculations performed with parameters adjusted on HT and EDC tests data are included.

As suggested in [8], damage and more precisely void nucleation is probably anisotropic in the non–hydrided material, maybe due to the material microstructure (*e.g.* grain morphology and distribution of precipitates) and crystallographic texture [49]. Furthermore, the damage kinetics due to hydride cracking measured after testing at room temperature have shown that, for hydrogen contents up to 800 wt. ppm, hydrides crack for a higher plastic strain under hoop tension than under axial tension (Fig. 4), possibly due to the morphology of hydrides and/or to the material texture. This anisotropy of damage cannot be represented by the model in its current form. Nevertheless, in order to illustrate the effect of damage anisotropy, HT tests were simulated by introducing a void nucleation around Laves phase precipitates delayed compared

to void nucleation determined under axial tension and by adjusting $\dot{f}_{nH}$, for the material hydrided at 400 wt. ppm, on the damage kinetics measured for HT and EDC tests: $p_{NLi} = 0.2$, $p_{NLf} = 1$ and $\epsilon_{NH} = 0.544$, the other parameters being unchanged. Note that strain values for void initiation (primarily from Laves phase particles) in the order of 0.12–0.16 and 0.20–0.27 were deduced by [23] from in–situ experiments performed at room temperature for wrought non–hydrided alpha–annealed and beta–treated Zircaloy–4, respectively. As shown in Figs. 9 and 11, a better agreement between experimental and calculated results is obtained with these parameters. The ductility of AT specimens is of course over–estimated with these parameters. These results illustrate the anisotropy of hydride cracking for moderate hydrogen contents. As previously done by [50], damage nucleation anisotropy could be accounted for in the model by introducing different critical strain values (at which void nucleation starts) for the different material directions.

In the case of the material hydrided at 1200 wt. ppm, strains at failure are correctly predicted by the model with parameters adjusted on AT tests results, in accordance with the similar damage kinetics measured under axial and hoop tension. Therefore, for high hydrogen contents, hydride cracking is isotropic, damage being expected to be in that case mainly controlled by the density of hydrides rather than by hydride morphology and/or material texture.

4.3. Expansion due to compression test

The EDC specimen is submitted at its mid–plane to a nearly uniaxial tension along the hoop direction [15]. A 2D plane–stress finite element model is used to simulate EDC tests. Only a part of the tube (r,θ) cross–section is represented. A geometrical flaw 1000 times smaller than the specimen thickness is introduced to force strain localization to occur in a given region without modifying the structure behavior. A radial displacement is imposed to the inner surface of the sample in order to simulate radial expansion of the pellet.

Calculations performed with the model parameters identified on AT tests results satisfactorily predict hoop strains at failure for the material hydrided at

about 800 wt. ppm and 1200 wt. ppm (Fig. 12). A good agreement is also obtained for the non–hydrided material and the material hydrided at 400 wt. ppm by using the parameters adjusted on the results of HT and EDC tests, both resulting in hoop tension of the cladding specimen. The ductility of the material non–hydrided or hydrided at 400 wt. ppm is logically under–estimated by the model with parameters tuned for AT tests. Once again, this suggests that void nucleation in the non–hydrided or moderately hydrided material is anisotropic.

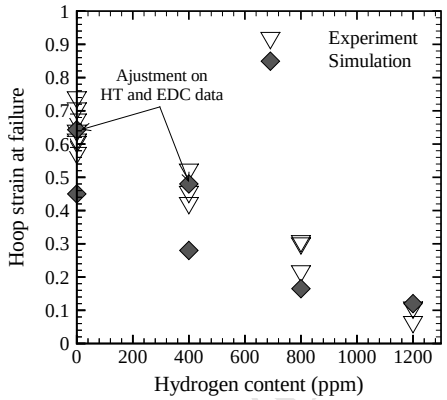

Figure 12: Experimental and calculated hoop strains at failure of EDC specimens tested at room temperature. Results of calculations performed with parameters adjusted on HT and EDC tests data are included.

According to the calculations, failure initiates, at room temperature for all tested hydrogen contents, at the specimen inner surface, where plastic strain is the highest (Fig. 13). The simulation predicts strain localization bands inclined at 45° from the hoop direction, in accordance with the macroscopic fracture plane observed for the non-hydrided material.

4.4. Hoop plane strain tensile test

Apart from the dimensions of the specimen and the D–shaped mandrels, the model used to simulate PST tests is similar to that already described for HT tests. A mesh size of $200\times200\times200\,\mu$m (instead of $100\times100\times100\,\mu$m for other tests) is used in order to keep reasonable computation times.

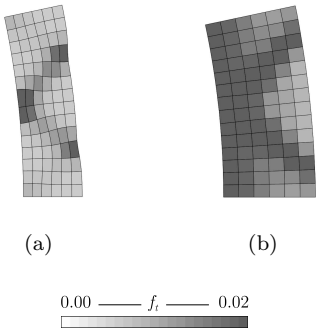

Figure 13: Total porosity fields calculated at crack initiation of EDC specimens tested at room temperature: (a) 25 °C, non–hydrided material, (b) 25 °C, material hydrided at 1200 wt. ppm.

Experimental plastic displacements at failure are lower than those calculated, probably due to the instability of the tensile machine and/or to an imperfect description of strain localization (highly dependent on strain hardening and strain rate sensitivity) and/or friction between the specimen and the D–shaped mandrels. The load level is under–estimated by the simulation at low plastic displacement levels. As already mentioned for HT tests, this may be attributed to an approximate description of the material strain hardening along the hoop direction, the proposed model not taking kinematic hardening into account. This may have an effect on the plastic displacement at which strain localization occurs but not on local strains at failure.

Hoop strain fields at the sample outer surface just before crack initiation are well reproduced by the simulations (Figs. 14 and 15). Thus, local strains at failure calculated with the model parameters identified from AT tests results are not under–estimated as for HT and EDC tests, although PST specimens are also predominantly loaded along the hoop direction. One can conclude that damage kinetics is faster during PST tests than during HT and EDC tests and that damage is influenced by the local stress state. Experimentally, failure of non–hydrided PST specimens tested at room temperature and hydrided specimens tested at 350 °C and 480 °C occurs in the plane strain area by through–thickness shear–dominated strain localization. When the stress state is dominated by

shearing, the volume of voids hardly evolves whereas their shape and orientation are significantly modified [8]. Then, although porosity in the strict sense does not evolve much, the deformation of voids has a strong effect on material softening [51, 52, 53]. The proposed model intrinsically reproduces the effect of triaxiality on void growth but does not account for this last phenomenon, associated with the effect of the Lode parameter (second measure of stress state in addition to stress triaxiality) [54]. Let us note that a phenomenological modification of the GTN model was proposed [53] in order to account for material softening under shear conditions, by introducing a dependence to the Lode parameter.

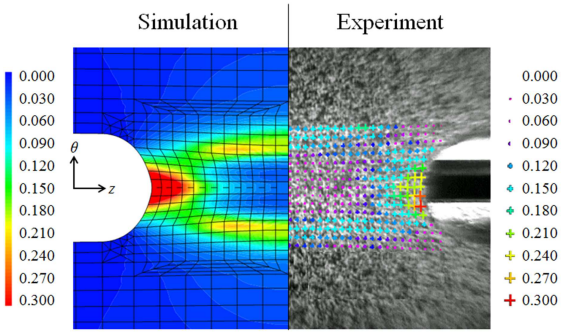

Figure 14: Green–Lagrange hoop strain fields calculated by FEA and measured by DIC just before failure at the outer surface of a non–hydrided PST specimen tested at room temperature.

For the hydrided material tested at room temperature, the simulations correctly predict crack initiation at the root of notches at the inner surface of the specimen (Fig. 16). This confirms that for these conditions, the assumption of independence on triaxiality of the damage model parameters is valid, at least for the studied range of triaxialities. According to the model, failure of the non–hydrided specimens tested at room temperature or at 480 °C initiates at the root of notches (Fig. 16) whereas it initiates in the plane strain area at the specimen inner surface during the experiments. Nevertheless, at crack initiation, calculated void volume fractions are close in the plane strain area and

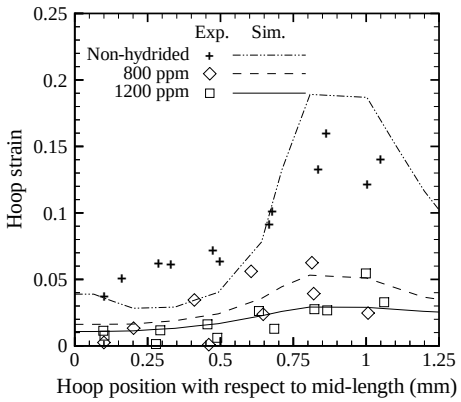

Figure 15: Hoop distribution (position with respect to the mid–length of the sample gauge section) of Green–Lagrange hoop strains calculated by FEA and measured by DIC at the onset of fracture, at the outer surface at the mid–width of PST specimens tested at room temperature.

at the root of notches. Then it is expected that the location of crack initiation could have been well predicted by adjusting model parameters for these specific tests and/or by taking into account material softening due to shear deformation of voids. In spite of these imperfections, strain and porosity fields at crack initiation are in agreement with the experimental specimen failure profiles [8].

5. Conclusions

A model has been proposed to describe the mechanical behavior and the ductile failure at 25, 350 and 480 °C of Zircaloy–4 cladding tubes as-received and hydrided up to 1200 wt. ppm (circumferential hydrides). The model is based on an extension of the Gurson–Tvergaard–Needleman model which includes a description of plastic anisotropy and viscoplasticity. Debonding of the interface between the Laves phase precipitates and the matrix and hydride cracking are taken into account to describe damage nucleation. Void nucleation around Laves phase precipitates is assumed to be controlled by plastic strain. The kinetics of damage nucleation by hydride cracking at room temperature is directly deduced from quantitative microstructural observations. It is expressed as a function of

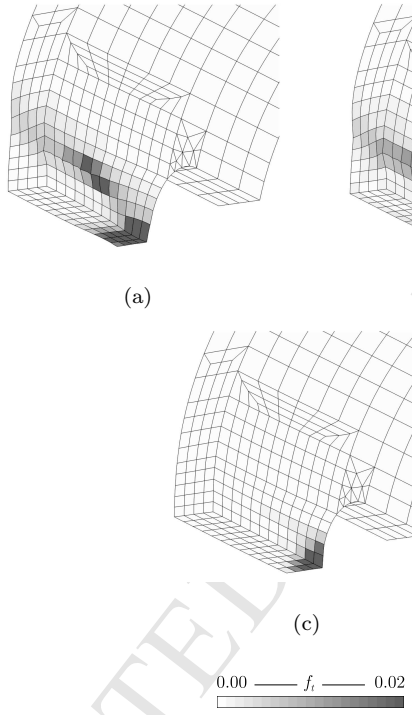

Figure 16: Total porosity fields calculated at crack initiation of PST specimens: (a) 25 °C, non–hydrided material, (b) 480 °C, non–hydrided material, (c) 25 °C, material hydrided at 1200 wt. ppm.

plastic strain, hydrogen content and temperature. The other model parameters were numerically identified on the basis of experimental tests results. It is shown that the critical porosity leading to void coalescence is lower when damage is associated with Laves phase precipitates than with hydrides.

The prediction capability of the model, used for finite element analysis, was evaluated by comparison to the results of axial tension, hoop tension, expansion due to compression and hoop plane strain tension experiments. The calculations satisfactorily reproduce the combined effects of hydrogen and temperature on the viscoplastic and the failure properties of the material. A better agreement between calculated and experimental results is obtained when considering that void nucleation, due to hydride cracking and to debonding of the interface between the Laves phase precipitates and the matrix, occurs for a higher plastic strain under hoop tension than under axial tension. Furthermore, the results suggest that damage is influenced by the stress state but also that stress triaxiality is maybe insufficient to describe all damage features, such as important softening under shear–dominated stress state. Since the anisotropy of damage and the potential effect of the Lode parameter on damage are not yet taken into account, the model cannot be fully predictive but can be regarded as a suitable tool for a better comprehension of the local damage mechanisms of the material and the global fracture modes of the specimens.

References

[1] P. Bossis, D. Pêcheur, K. Hanifi, J. Thomazet, M. Blat, Comparison of the high burn–up corrosion on M5 and low tin Zircaloy–4, Journal of ASTM International 3 (2005) 494–525.

[2] A. Hellouin de Menibus, J. Sercombe, Q. Auzoux, C. Poussard, Thermo-mechanical loading applied on the cladding tube during the pellet cladding mechanical interaction phase of a rapid reactivity initiated accident, Journal of Nuclear Materials 453 (2014) 210–213.

[3] J. Desquines, D. Koss, A. Motta, B. Cazalis, M. Petit, The issue of stress state during mechanical tests to assess cladding performance during a reactivity-initiated accident (RIA), Journal of Nuclear Materials 412 (2) (2011) 250–267.

[4] J. Papin, B. Cazalis, J. Frizonnet, J. Desquines, F. Lemoine, V. Georgenthum, F. Lamare, M. Petit, Summary and interpretation of the CABRI REP–Na program, Nuclear Technology 157 (3) (2007) 230–250.

[5] T. Fuketa, 2.22 — Transient response of LWR fuels (RIA), Comprehensive Nuclear Materials 2 (2012) 579–593.

[6] F. Yunchang, D. Koss, The influence of multiaxial states of stress on the hydrogen embrittlement of zirconium alloy sheet, Metallurgical Transactions A 16 (1985) 675–681.

[7] B. Cazalis, J. Desquines, C. Poussard, M. Petit, Y. Monerie, C. Bernaudat, P. Yvon, X. Averty, The PROMETRA program: Fuel cladding mechanical behavior under high strain rate, Nuclear Technology 157 (2007) 215–229.

[8] M. Le Saux, J. Besson, S. Carassou, C. Poussard, X. Averty, Behavior and failure of uniformly hydrided Zircaloy–4 fuel claddings between 25 °C and 480 °C under various stress states, including RIA loading conditions, Engineering Failure Analysis 17 (2010) 683–700.

[9] A. Hellouin de Menibus, Q. Auzoux, P. Mongabure, V. Macdonald, T. Le Jolu, J. Besson, J. Crepin, Fracture of Zircaloy–4 cladding tubes with or without hydride blisters in uniaxial to plane strain conditions with standard and optimized expansion due to compression tests, Materials Science and Engineering A 604 (2014) 57–66.

[10] M. Cunningham, C. Beyer, P. Medvedev, G. Berna, FRAPTRAN: A computer code for the transient analysis of oxide fuel rods, Report NUREG/CR-6739, Vol. 1, PNNL-13576, Nuclear Regulatory Commission and Pacific Northwest National Laboratory (2001).

[11] Y. Rashid, R. Dunham, R. Montgomery, Fuel analysis and licensing code: FALCON MOD01. Volume 1: Theoretical and numerical bases, Technical Report ANA-04-0666, EPRI, Palo Alto, CA (2004).

[12] C. Bernaudat, S. Cambier, J. Guion, S. Benjamin, An analytical criterion to prevent PCMI fuel rod cladding failure during ria transients, in: Water Reactor Fuel Performance Meeting, Paris, France, 2009, pp. 497–506.

[13] A. Moal, V. Georgenthum, O. Marchand, SCANAIR: A transient fuel performance code: Part one: General modelling description, Nuclear Engineering and Design 480 (2014) 150–171.

[14] T. Link, T. Koss, A. Motta, Failure of Zircaloy cladding under transverse plane-strain deformation, Nuclear Engineering and Design 186 (1998) 379–394.

[15] M. Le Saux, C. Poussard, X. Averty, C. Sainte Catherine, J. Besson, High temperature expansion due to compression test for the determination of a cladding material failure criterion under RIA loading conditions, in: International Topical Meeting on Light Water Reactor Fuel Performance, San Francisco, California, 2007, pp. 526–535.

[16] S. Leclercq, A. Parrot, M. Leroy, Failure characteristics of cladding tubes under RIA conditions, Nuclear Engineering and Design 238 (9) (2008) 2206–2218.

[17] J. Lemaitre, A continuous damage mechanics model for ductile fracture, Journal of Engineering Materials and Technology 107 (1985) 83–89.

[18] G. Rousselier, Ductile fracture models and their potential in local approach of fracture, Nuclear Engineering and Design 105 (1987) 97–111.

[19] A. Gurson, Continuum theory of ductile rupture by void nucleation and growth: Part I – Yield criteria and flow rules for porous ductile media, Journal of Engineering Materials and Technology 99 (1977) 2–15.

[20] V. Tvergaard, A. Needleman, Analysis of cup–cone fracture in a round tensile bar, Acta Metallurgica 32 (1984) 157–169.

[21] V. Tvergaard, Material failure by void growth to coalescence, Advances in Applied Mechanics 27 (1990) 83–151.

[22] J. Rice, D. Tracey, On the ductile enlargement of voids in triaxial stress, Journal of the Mechanics and Physics of Solids 17 (1969) 201–217.

[23] B. Cockeram, K. Chan, In situ studies and modeling of the deformation and fracture mechanism for wrought Zircaloy–4 and Zircaloy–2 as a function of stress-state, Journal of Nuclear Materials 434 (1-3) (2013) 97–123.

[24] Q. Chen, J. Ostien, G. Hansen, Development of a used fuel cladding damage model incorporating circumferential and radial hydride responses, Journal of Nuclear Materials 447 (1-3) (2014) 292–303.

[25] Y. Udagawa, T. Mihara, T. Sugiyama, M. Suzuki, M. Amaya, Simulation of the fracture behavior of Zircaloy-4 cladding under reactivity-initiated accident conditions with a damage mechanics model combined with fuel performance codes FEMAXI-7 and RANNS, Journal of Nuclear Science and Technology 51 (2) (2014) 208–219.

[26] B. Williams, S. St Lawrence, B. Leitch, Comparison of the measured and predicted crack propagation behaviour of Zr-2.5Nb pressure tube material, Engineering Fracture Mechanics 78 (2011) 3135–3152.

[27] M. Grange, J. Besson, E. Andrieu, An anisotropic Gurson type model to represent the ductile rupture of hydrided Zircaloy–4 sheets, Internal Journal of Fracture 105 (2000) 273–293.

[28] V. Tvergaard, Influence of voids on shear band instabilities under plane strain conditions, International Journal of Fracture 17 (4) (1981) 389–407.

[29] R. Hill, The Mathematical Theory of Plasticity, Clarendon Press, Oxford, 1950.

[30] H. Chu, S. Wu, K. Chien, R. Kuo, Effect of radial hydrides on the axial and hoop mechanical properties of Zircaloy–4 cladding, Journal of Nuclear Materials 362 (2007) 93–103.

[31] M. Gologanu, J. Leblond, J. Devaux, Approximate models for ductile metals containing non-spherical voids – case of axisymmetric oblate ellipsoidal cavities, Journal of Engineering Materials And Technology 116 (1994) 290–297.

[32] J. Besson, L. Devillers-Guerville, A. Pineau, Modeling of scatter and size effect in ductile fracture: application to thermal embrittlement of duplex stainless steels, Engineering Fracture Mechanics 67 (2000) 169–190.

[33] J. Besson, C. Guillemer-Neel, An extension of the Green and Gurson models to kinematic hardening, Mechanics of Materials 35 (2003) 1–18.

[34] G. Perrin, J. Leblond, Accelerated void growth in porous ductile solids containing two populations of cavities, International Journal of Plasticity 16 (1) (2000) 91–120.

[35] D. Fabrègue, T. Pardoen, A constitutive model for elastoplastic solids containing primary and secondary voids, Journal of the Mechanics and Physics of Solids 56 (3) (2008) 719–741.

[36] M. Le Saux, J. Besson, S. Carassou, C. Poussard, X. Averty, A model to describe the anisotropic viscoplastic mechanical behavior of fresh and irradiated Zircaloy–4 fuel claddings under RIA loading conditions, Journal of Nuclear Materials 378 (2008) 60–69.

[37] M. Grange, J. Besson, E. Andrieu, Anisotropic behavior and rupture of hydrided Zircaloy–4 sheets, Metallurgical and Materials Transactions A 31 (2000) 679–690.

[38] J. Kearns, Terminal solubility and partitioning of hydrogen in the alpha phase of zirconium, Zircaloy–2 and Zircaloy–4, Journal of Nuclear Materials 22 (3) (1967) 292–303.

[39] A. Hellouin de Menibus, Q. Auzoux, J. Besson, J. Crépin, Temperature increase of Zircaloy–4 cladding tubes due to plastic heat dissipation during tensile tests at 0.1–10 s^{-1} strain rates, Journal of Nuclear Materials 454 (1-3) (2014) 247–254.

[40] D. Charquet, R. Hahn, E. Ortlieb, J. Gros, J. Wadier, Solubility limits and formation of intermetallic precipitates in ZrSnFeCr, in: 8th International Symposium on Zirconium in the Nuclear Industry, ASTM STP 1023, Philadelphia, USA, 1989, pp. 405–422.

[41] K. Erwin, O. Delaire, A. Motta, Y. Chu, D. Mancini, R. Birtcher, Observation of second–phase particles in bulk zirconium alloys using synchroton radiation, Journal of Nuclear Materials 294 (3) (2001) 299–304.

[42] C. Chu, A. Needleman, Void nucleation effects in biaxially stretched sheets, Journal of Engineering Materials and Technology 102 (1980) 249–256.

[43] G. Fearnehough, A. Cowan, The effect of hydrogen and strain rate on the "ductile-brittle" behaviour of Zircaloy, Journal of Nuclear Materials 22 (1967) 127–147.

[44] J. Huang, S. Huang, Effect of hydrogen contents on the mechanical properties of Zircaloy–4, Journal of Nuclear Materials 208 (1994) 166–179.

[45] S. Shi, M. Puls, Fracture strength of hydride precipitates in Zr–2.5Nb alloys, Journal of Nuclear Materials 275 (1999) 312–317.

[46] U. Viswanathan, R. Singh, C. Basak, S. Anantharaman, K. Sahoo, Evaluation of effect of hydrogen on toughness of Zircaloy–2 by instrumented drop weight impact testing, Journal of Nuclear Materials 350 (3) (2006) 310–319.

[47] Z. Zhang, C. Thaulow, J. Odegard, A complete Gurson model approach for ductile fracture, Engineering Fracture Mechanics 67 (2000) 155–168.

[48] F. Bron, J. Besson, Simulation of the ductile tearing for two grades of 2024 aluminum alloy thin sheets, Engineering Fracture Mechanics 73 (2006) 1531–1552.

[49] S. Caré, A. Zaoui, Cavitation at triple nodes in α–zirconium polycrystals, Acta Materialia 44 (4) (1996) 1323–1336.

[50] T. Morgeneyer, J. Besson, H. Proudhon, M. Starink, I. Sinclair, Experimental and numerical analysis of toughness anisotropy in AA2139 al alloy sheet, Acta Materialia 57 (13) (2009) 3902–3915.

[51] K. Zhang, J. Bai, D. François, Numerical analysis of the influence of the Lode parameter on void growth, Journal of Solids and Structures 38 (2001) 5847–5856.

[52] I. Barsoum, J. Faleskog, Rupture mechanisms in combined tension and shear – Micromechanics, International Journal of Solids and Structures 44 (2007) 5481–5498.

[53] K. Nahshon, J. Hutchinson, Modification of the Gurson model for shear failure, European Journal of Mechanics A/Solids 27 (2008) 1–17.

[54] W. Lode, The influence of the intermediate principal stress on yielding and failure of iron, copper and nickel, Engineering Mathematical Mechanics 5 (1925) 142.

List of Figures

List of Tables